Journal of Experimental Nanoscience,
Vol. 1, No. 1, March 2006, 29–50

Light-emitting silicon-rich nitride systems and photonic structures

L. DAL NEGRO*†, J. H. YI†, M. HILTUNEN†⊥, J. MICHEL†, L. C. KIMERLING†, S. HAMEL‡, A. J. WILLIAMSON‡, G. GALLI‡, T.-W. F. CHANG§, V. SUKHOVATKIN§ and E. H. SARGENT§

†Massachusetts Institute of Technology, 77 Massachusetts Avenue, Cambridge, MA 02139, USA
‡Lawrence Livermore National Laboratory, Livermore, CA 94550, USA
§University of Toronto, 10 King's College Road, Toronto, Canada, M5S 3G4

(*Received October 2005; in final form November 2005*)

In this paper we report recent results on the optoelectronic properties of silicon-rich nitride (SRN), a novel material for microphotonics applications compatible with silicon technology. We have investigated optical emission, energy transfer phenomena to erbium ions and PbS colloidal quantum dots in SRN films and grown active photonic SRN structures. The optical properties of the films were studied by micro-Raman and photoluminescence spectroscopy and, as confirmed by transmission electron microscopy analysis, indicate the presence of small (1–2 nm) Si clusters characterized by efficient (7% quantum efficiency at room temperature), broad-band and near-infrared emission with very large absorption/emission Stokes shift. Time and temperature resolved photoluminescence measurements demonstrate nanosecond-fast, wavelength-dependent recombination dynamics with negligible light emission thermal quenching from 4 to 330 K. First-principles simulations of 1 nm size crystalline and amorphous silicon dots show that nitrogen atoms bonded to the surface of nanometre silicon clusters play a crucial role in the emission mechanism of SRN films. In addition, we show that SRN is a suitable material for the fabrication of light-emitting complex photonic crystals and novel waveguide structures based on resonant transmission of localized light states in aperiodic dielectrics. The versatility of light-emitting SRN systems can provide alternative routes towards the fabrication of optically active CMOS devices.

Keywords: Nanocrystals; Light emission; Nitride materials
PACS: 78.67.Bf Nanocrystals and nanoparticles; 78.55.-m Light emission; 77.84.Bw Nitride materials

1. Introduction

Silicon has recently been shown to be a powerful material for integrated optics [1–3], modulation [4], switching [5], and even lasing [6,7]. However, it has not yet proved to be an efficient light-emitting material. Light emission in bulk silicon (Si) originates from

*Corresponding author. Department of Electrical and Computer Engineering, Boston University, 8 Saint Mary's Street, Room 2825, Boston, MA 02215-2421. Email: dalnegro@mit.edu; Alternate email: dalnegro@bu.edu
⊥On leave from: VTT Electronics, Kaitovayla 1, 90570 Oulu, Finland

Journal of Experimental Nanoscience
ISSN 1745-8080 print/ISSN 1745-8099 online © 2006 Taylor & Francis
http://www.tandf.co.uk/journals
DOI: 10.1080/17458080500469310

a low-probability phonon-mediated transition that unfavourably competes with fast non-radiative recombination paths. The lack of efficient light emission in bulk Si has, up to now, hampered the monolithic integration of electronic and optical devices on mass-produced Si chips. However, several technological routes are now open to turn Si into a more efficient light-emitting material [8–12]. Recently, new Si nanostructures have been synthesized that take advantage of quantum confinement to dramatically improve light generation efficiency. High emission efficiencies up to 23% under optical excitation have been reported in porous Si after high-pressure water vapour annealing [13] and sizeable optical gain has recently been demonstrated in Si nanocrystals (Si-nc's) embedded in SiO_2 matrices [14–19], opening the race towards the fabrication of a fully Si-based laser [11]. Moreover, it has been recently discovered that Si-nc's act as efficient energy sensitizers for rare-earth ions, particularly erbium (Er) ions, allowing broad-band pumping of 1.55 m light emission with almost three orders of magnitude enhanced pumping efficiency [20–22]. Despite all these exciting results, porous Si and Si-nc embedded in SiO_2 matrices are not suitable for the fabrication of reliable, optically efficient and stable electrically driven light sources due to the insulating SiO_2 barriers and the slow exciton recombination lifetime (10–100 s). Therefore, alternative Si-compatible (or CMOS compatible) approaches that can yield fast (ns), efficient and stable electrical excitation need to be investigated. An intriguing possibility would be the nucleation of Si nanoclusters in dielectric matrices with smaller bandgap than SiO_2 and more favourable electrical properties. Following this approach, visible and near-infrared light-emitting Si clusters embedded in amorphous Si nitride matrices have recently been demonstrated [23–26]. Here we will present our main experimental as well as theoretical results on the optical emission properties of thermally annealed Si-rich silicon nitride (SRN), new energy transfer phenomena involving erbium ions and PbS colloidal quantum dots and we discuss our results on SRN-based light-emitting photonic structures.

2. Experimental details

Si-rich nitride (SRN) samples were fabricated through plasma enhanced chemical vapour deposition (PE-CVD) using an Applied Materials Centura DxZ chamber with SiH_4 and N_2 as precursors and a substrate temperature of 400°C. In order to induce the nucleation and growth of small Si clusters all the SRN films were annealed in N_2-rich atmosphere for 10 minutes at temperatures ranging between 600 and 900°C. Additionally, SRN films were also deposited for comparison by direct sputtering from Si and Si_3N_4 targets and annealed in the same conditions. Er-doped SRN films (Er : SRN) were fabricated by direct magnetron co-sputtering from Er, Si and Si_3N_4 targets. Reference Si-rich SiO_2 samples (SRO) were deposited through a reactive RF magnetron in an O_2/Ar atmosphere using a Kurt J. Lesker Co. CMS 18 sputtering system. All the samples have been deposited on transparent fused silica substrates and annealed at different temperatures ranging from 500 to 1250°C. In the investigation of energy transfer from SRN to PbS quantum dots, the PbS quantum dots used were produced by a colloidal synthesis [27]. As synthesized, each PbS quantum dot is capped by a layer of oleate ligand. To enhance the interaction strength between the

PbS quantum dots and their surrounding materials, the 2 nm long oleate ligands are replaced by the 0.5 nm long butylamine ligands through a solution-based procedure. Micro-Raman measurements were performed at 514 nm using a Kaiser Optical Systems Raman spectrometer with confocal microprobe. Optical transmission experiments were performed using a commercial Cary 5E double beam spectrophotometer equipped with a PbS detector (for the near-infrared range) or a Hamamatsu photomultiplier tube (for the visible range). Room-temperature photoluminescence (PL) experiments were performed using a 488 nm Ar pump laser and a liquid nitrogen cooled InGaAs photomultiplier tube. PL decay measurements were obtained using the 457 nm line of a nitrogen pumped dye laser (pulse width 1 ns, 10 Hz repetition rate).

3. Optical emission properties of silicon-rich nitride

The study and the optimization of light emission from Si-rich nitride (SRN) amorphous materials can have a significant impact for silicon microphotonics due to the combination of efficient light generation and more favourable electrical injection with respect to larger bandgap SRO-based materials. Visible, light-emitting electroluminescent devices with 2% efficiency at room temperature [24] and near-infrared emitting photonic structures [25] have already been demonstrated following this approach.

In the following, we will review our principal results concerning the optical emission properties of thermally annealed SRN films deposited by PE-CVD and we will directly compare the emission efficiency of SRN and Si-rich oxide samples (SRO) deposited by magnetron sputtering. Figure 1 summarizes the effect of film stoichiometry (as measured through the sample refractive index variations associated with the excess Si content) and post-deposition annealing temperature on the emission intensity of SRN and SRO samples. In figure 1(a,b) we show the trends of the integrated PL intensity versus the SRN and SRO film refractive indices, as measured at 1.55 m by the prism coupling technique. Figure 1(c,d) shows the integrated PL intensity versus the post-deposition annealing temperatures for the same materials. The result of our systematic study shows that the best light emission performances are obtained for SRN samples with the highest Si content (refractive index $n = 2.23$), after thermal annealing at 700°C for 10 min. For comparison, figure 1(b,d) shows the light emission optimization trends versus film refractive index and annealing temperature (fixed time at 1 hour) for SRO films deposited by magnetron sputtering. In this case, we found that the integral PL intensity is maximized for films with 1.7 refractive index annealed at 1150°C for 1 hour, as a result of a competitive interplay between the nucleation of luminescent Si clusters with different sizes, emission efficiencies and clusters density. However, our data indicate that a major difference exists between SRN and SRO light-emitting systems. In fact, we have found that the optimum annealing time (1 hour) and temperature (1150°C) required to maximize the Si-nc light emission in oxide systems are much larger than what is required to activate efficient light emission in SRN systems. This suggests that the growth kinetics in nitride films favours the formation of smaller Si clusters at a faster rate and for lower supersaturation than for the SRO case. To confirm this assumption, we have performed micro-Raman and transmission electron

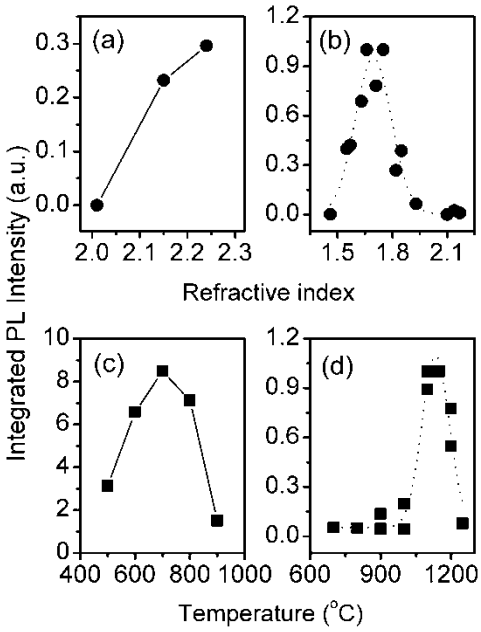

Figure 1. (a) Integrated PL intensity versus refractive index for SRN films annealed at 700°C for 10 min. (b) Integrated PL intensity versus refractive index for SRO films annealed at 1100°C for 60 min. (c) Integrated PL intensity versus annealing temperature for SRN films with $n = 2.2$ refractive index and annealed for 10 min. (d) Integrated PL intensity versus annealing temperature for SRO films with $n = 1.7$ refractive index and annealed for 60 min.

microscopy (TEM) analysis on the best emitting SRN and SRO samples. Figure 2(a) shows the micro-Raman spectra of a reference bulk silicon (c-Si) sample (dash-dot), an as-deposited (not annealed) SRN sample produced by direct magnetron sputtering (dash line) and a thermally annealed (700°C, 10 min) PE-CVD deposited sample (solid line). We see that for sputtered SRN samples (with no substrate heating) only a broad Raman band due to an amorphous Si network is observed (dash line). On the contrary, in the case of thermally annealed SRN samples deposited by PE-CVD, a broadened, asymmetric and shifted Raman peak (with respect to bulk Si) can be clearly observed (solid line). Additionally we notice that for the PE-CVD sample, the two-phonon optical (900 cm^{-1}) and acoustical (300 cm^{-1}) scattering bands are strongly enhanced with respect to both the bulk Si and the sputtered SRN samples. The presence of a significantly shifted (15 cm^{-1}) and asymmetrized one-phonon Raman peak for PE-CVD deposited SRN is direct evidence of the formation of small Si clusters embedded in the amorphous silicon nitride matrix. The physical origin of the broadened Si peak is related to the uncertainty in the Si-cluster phonon momentum q that allows modes with $q \neq 0$ to contribute in the Raman spectrum. This general physical picture, referred to as the phonon bottleneck, can be quantitatively described within a phenomenological model that accounts for the lineshape of the TO one-phonon modes of quantum confined Si clusters [28]. In figure 2(b) we show the simulated one-phonon Raman lineshape corresponding to Si clusters with decreasing size.

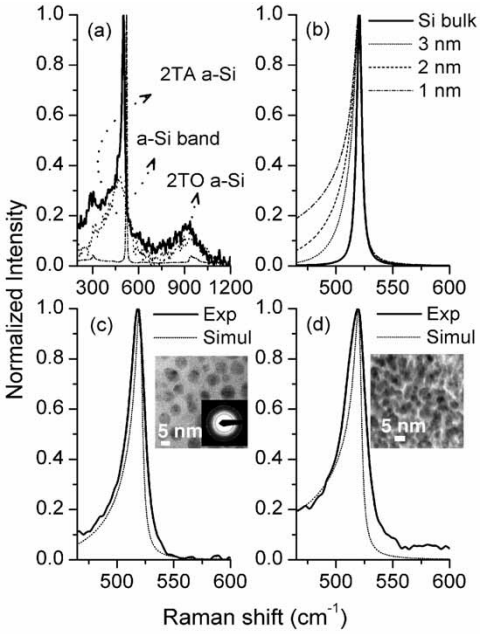

Figure 2. (a) Micro-Raman spectra of crystalline silicon (dash-dot line), PE-CVD deposited SRN with $n = 2.2$ and annealed at 700°C for 10 min (solid line), SRN deposited by magnetron sputtering unannealed (dot line). (b) Simulations of the one-phonon nanocrystalline Raman spectrum for different dot sizes indicated in the figure. (c) Micro-Raman spectrum of silicon nanocrystals embedded in SiO_2 (solid line). Theoretical simulation assuming 3 nm average crystal radius (dot line). The inset shows a cross-section TEM image where the dark spots are the silicon nanocrystals. (d) Micro-Raman spectrum of silicon nanocrystals embedded in amorphous Si_3N_4 (solid line). Theoretical simulation assuming 2 nm average crystal size (dot line). The inset shows a cross-section TEM image where the dark spots are the silicon nanocrystals.

The one-phonon Raman lineshapes can be easily obtained by calculating the integral transform [29]:

$$I(\omega) = \int_0^1 \frac{e^{-qL^2/4a^2}}{[\omega - \omega(q)]^2 + (\Gamma_0/2)^2} d^3q \tag{1}$$

where L is the average Si-nc radius, Γ_0 is the linewidth of the LO bulk Si phonon, a is the Si lattice constant and we have used the phonon dispersion of the bulk material as given by the relation $\omega^2(q) = A + B\cos(\pi q/2)$ with $A = 1.714 \times 10^5\ \mathrm{cm}^{-2}$ and $B = 1.000 \times 10^5\ \mathrm{cm}^{-2}$ [29, 30]. This phenomenological approach allows us to simulate the experimental Raman data and to estimate an average size for the quantum confined scattering particles. We have applied this procedure to SRO samples (annealed at 1100°C for 1 h) and SRN samples (annealed at 700°C for 10 min) and we have checked the consistency with the results of TEM analysis (figure 2c,d). In the case of SRO samples, we estimate an average radius of ~3 nm, in good agreement with the TEM image (figure 2c). In the case of thermally annealed SRN, the micro-Raman data are compatible with the presence of smaller Si clusters with an estimated size less than 2 nm,

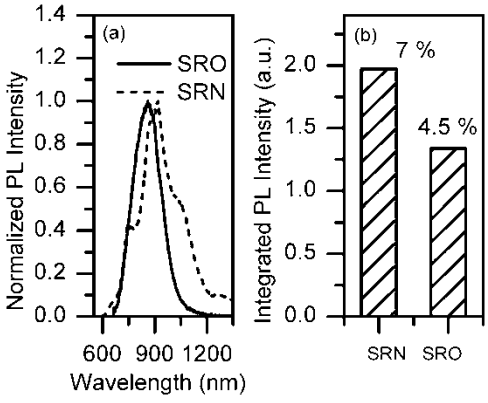

Figure 3. (a) Normalized PL spectra of the optimized ($n = 1.7$, annealed for 60 min at 1100°C) SRO film (solid line) and the best emitting ($n = 2.2$, annealed for 10 min at 700°C) SRN film (dash line). Pump power 5 mW at 488 nm. The oscillations in the SRN emission spectrum are due to interference effects related to the finite sample thickness (700 nm). (b) Histograms of the integrated PL intensity of the two compared SRN and SRO samples.

as fitted within the phonon confinement Raman model (see figure 2d). In addition, by TEM analysis (figure 2d), we can demonstrate the presence of small silicon clusters in thermally annealed SRN, whose average size is compatible with 1–2 nm.

In order to quantitatively compare the emission efficiency of SRO versus SRN light-emitting systems we have measured the external PL quantum efficiency (PLQE) of the best emitting SRN film ($n = 2.2$, 700°C, 10 min) and SRO samples ($n = 1.7$, 1150°C, 1 hour). Figure 3(a) shows the normalized room-temperature emission spectra of the SRO (solid line) and SRN (dash line) samples that we have compared. We notice that the emission spectra of the two samples are very similar and consist of broad emission bands centred around 900 nm. A PLQE of 7% was measured for the SRN samples, following the procedure described in [31, 32]. In the case of the optimized SRO reference samples, a PLQE of 4.5% was obtained. The histograms of the corresponding integrated PL intensities are shown in figure 3(b). In figure 4 we show a direct comparison of the 7% efficient near-infrared SRN emission spectrum and the optical transmission spectrum. It is clear that the emission band (figure 4a) is strongly Stokes-shifted with respect to the onset of the measured absorption edge (figure 4b), suggesting the strongly localized nature of the emitting centers. In the next section we will show that first-principles theoretical calculations indicate that light emission in SRN originates from strongly localized, nitrogen-related exciton states at the surface of small (1–2 nm) Si clusters embedded in an amorphous Si_3N_4 network. Figure 5 shows the measured wavelength dispersion of the PL lifetime of the best emitting SRN sample. We have found that the SRN lifetime is described by a double exponential function with a resolution limited subnanosecond fast decay component and a longer decay component that ranges between 1 and 5 ns, depending on the observation wavelength [33]. The inset shows two representative PL decay traces. The temperature behaviour of the SRN light emission is shown in figure 6. We found that the SRN emission shows negligible temperature quenching (approximately a factor of 4) over

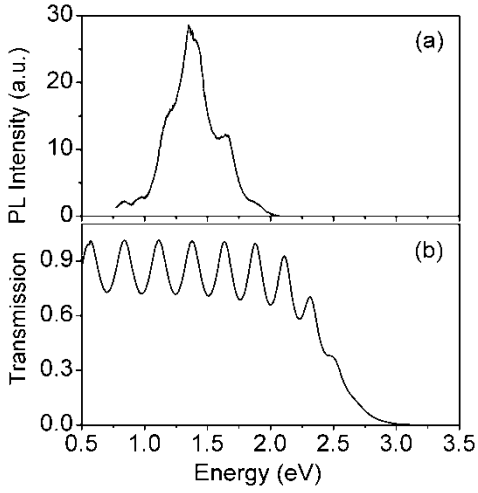

Figure 4. (a) Room-temperature photoluminescence (PL) spectra of SRN samples annealed for 10 min at 700°C. Pump power 5 mW at 488 nm. (b) Typical transmission spectrum of SRN sample annealed at 700°C. The oscillations in the spectrum are due to Fabry–Perot wave interference related to the finite sample thickness (700 nm).

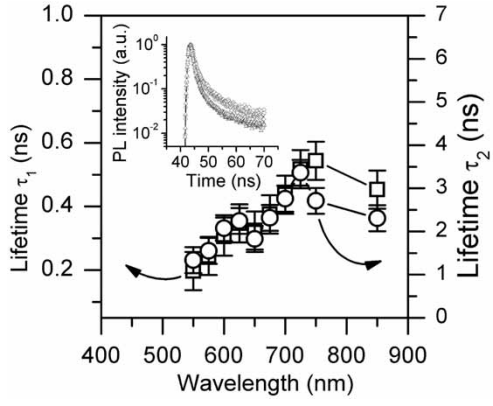

Figure 5. (a) PL emission lifetime versus observation wavelength for the best emitting SRN sample ($n = 2.2$, annealed for 10 min at 700°C). (Inset) Typical decay curves observed at 710 nm (open triangles) and 810 nm (open diamonds) fitted using double exponential decay curves (solid lines).

a wide temperature range from 4 K up to 330 K. In addition, no appreciable emission lineshape modifications have been observed (figure 6).

The temperature-dependent PL data can be described by using a simple phenomenological model based on the thermal ionization of localized carriers from a radiative nitrogen defect state, as in [34]. However, we associate the microscopic nature of the radiative nitrogen defects suggested in [34] to the strongly localized energy state introduced by surface nitrogen bridging configurations within the molecular bandgap of small Si clusters embedded in the nitride matrix [26], as will be discussed

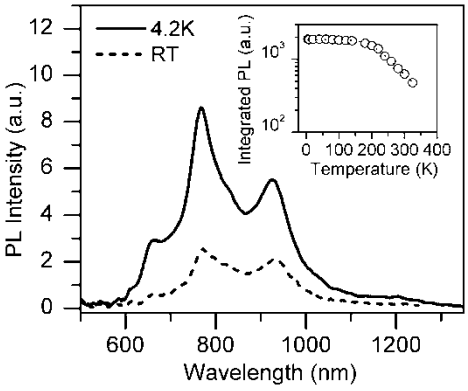

Figure 6. Room-temperature (dash line) and 4.2 K (solid line) SRN emission spectra. (Inset) Integrated PL intensity versus temperature for the best emitting SRN sample ($n = 2.2$, annealed for 10 min at 700°C).

in the next section. According to this interpretation, the fast subnanosecond PL decay component is associated with a non-radiative exciton trapping time on the nitrogen sites while the longer (ns) decay results from the localized exciton recombination time.

4. Silicon nanoclusters embedded in silicon nitride: theoretical modelling

Understanding the interaction between a Si nanocluster and the surrounding SRN matrix is extremely complex due to the unknown structure of the cluster and the various types of Si–N bonds that may be present at the interface between the cluster and the matrix. To investigate how the structure of the cluster and bonds at the interface can influence the optical properties of SRN materials, we performed a series of density functional theory (DFT) calculations,† within the local density approximation [36] (LDA) of the structural, electronic and optical properties of silicon nanoclusters with single nitrogen atoms bonded to their surface and in their core in different configurations. The structures are summarized in table 1 and shown in figure 7. Structures (a)–(g) have a diamond crystalline core. Structures (h)–(i) have an amorphous core generated using an *ab initio* molecular dynamics simulations [37]. Structure (a), $Si_{35}H_{36}$, is our reference crystalline structure. Structure (h) is our reference hydrogen terminated amorphous silicon cluster, $Si_{30}H_{20}$. It has lower hydrogen content than structure (a) due to the reconstruction of its surface. For all N-doped clusters but (e), in keeping with known molecules containing N, Si and H atoms such as disilazane and trisilylamine or studies of the dissociative adsorption of ammonia on silicon surfaces [38, 39], the nitrogen atoms attached to these clusters are three-fold coordinated. In structures (b) and (i), a hydrogen atom is replaced with an amine group. Structure (b) is similar to $Si_{35}H_{35}OH$ considered in [40], where a surface H

† The Qbox [36] code was used for the structural relaxation and the ABINIT [37] code was used to evaluate gaps and oscillator strength. All calculations use norm-conserving, Troullier–Martins pseudopotentials for the core electrons and a plane-wave basis with a 70 Ry cutoff [35]. The ABINIT code is a common project of the Université Catholique de Louvain, Corning Incorporated, and other contributors: URL http://www.abinit.org

Table 1. Calculated LDA and PBE optical gaps, and radiative lifetimes corresponding to different Si nanoclusters.

Structure	LDA gap (eV)	Lifetimes (ns)
(a) $Si_{35}H_{36}$ – reference crystalline structure	3.4	10^2
(b) $Si_{35}H_{35}NH_2$ – NH_2 substituting H	3.0	10^3
(c) $Si_{34}H_{35}N$ – N substituting SiH	2.8	10^2
(d) $Si_{34}H_{34}NH$ – NH substituting SiH_2	2.7, 2.9	forbid.*, 10^3
(e) $Si_{35}H_{34}NH$ – NH substituting 2H	2.4	10^2
(f) $Si_{35}H_{34}NH$ – Si–NH–Si bridge	2.2	10^1
(g) $Si_{34}H_{37}NH$ – N in the core of the cluster	2.7	10^2
(h) a-$Si_{30}H_{22}$ – reference amorphous structure	2.2	10^2
(i) a-$Si_{30}H_{21}NH_2$ – NH_2 substituting H	2.1	10^2
(j) a-$Si_{30}H_{20}NH$ – Si–NH–Si bridge	1.8	10^4

*In (d), the HOMO–LUMO transition is forbidden and we quote the lifetime of the HOMO–LUMO + 1 transition at 2.9 eV.

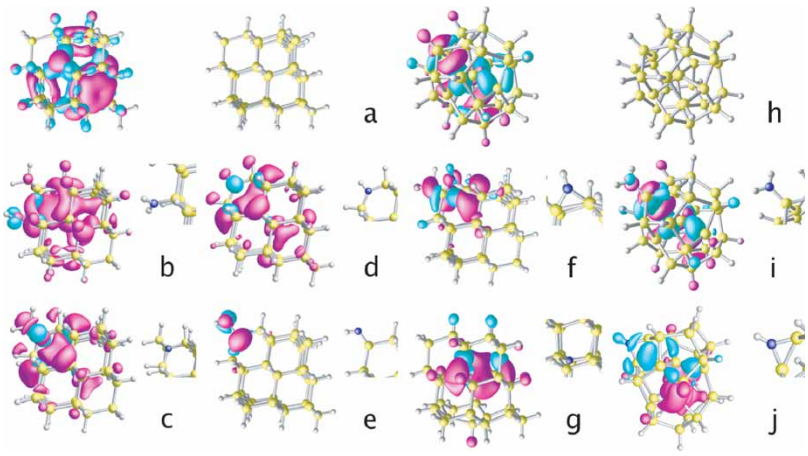

Figure 7. Isosurface plots of the density of the highest occupied molecular orbital (HOMO) in cyan and lowest unoccupied molecular orbital (LUMO) in magenta. Silicon atoms are yellow, nitrogen atoms are blue, and hydrogen atoms are light grey. The isosurfaces contain 30% of an electron charge. For the reference structures (a) and (h) the full structure is shown. For all other structures the inset plots show a zoom-in of the nitrogen containing groups on the surfaces of the clusters. This figure is available in colour online.

is replaced with either an OH group and also similar to the end product of the dissociative adsorption of ammonia on silicon surfaces. In structure (d) an SiH_2 group is replaced with an NH group, while in (f) an NH group is bonded to two neighbouring silicon atoms, forming in both clusters a bridged Si–NH–Si structure reminiscent of disilazane. The important difference between these two clusters is that in (f) the two Si are bonded to each other, producing a Si–N–Si angle that is much smaller in (f), 83°, than in (d), 131°, which is closer to the experimental value of 127.7° of dizilazane [41]. Structure (j) is the amorphous version of the Si–NH–Si bridged structure (f). In structure (c) a SiH group is replaced by a N atom, while in structure (g) a Si atom in the core of the cluster is replaced with a N. Both clusters show N bonded to three Si, much like in trisilylamine. Finally, structure (e) has a surface Si=NH double bond,

comparable to $Si_{35}H_{34}O$ in [40], which has a double bonded surface Si=O group. For each cluster, the atomic coordinates were relaxed to the closest local minimum of the potential energy surface and then the optoelectronic properties were calculated for the relaxed structure.

To determine which structure(s) are most likely to be responsible for the luminescence observed in SRN we calculated the energy gap between the highest occupied molecular orbital (HOMO), and lowest unoccupied molecular orbital (LUMO) and the radiative lifetime for the HOMO–LUMO transition. As the HOMO and LUMO orbitals will be shown to be localized around nitrogen atoms on the surface of the nanoclusters (see figure 7), we expect that the calculated trends between the gaps and radiative lifetimes of the different structures will be insensitive to the exact size of the clusters and the structure of the surrounding SRN matrix. This effect was observed in nanoclusters terminated with oxygen [40], where the localized nature of the HOMO and LUMO orbital gave rise to a weak size dependence of the gap. In addition, as the measured luminescence is bright and weakly temperature dependent, we anticipate that comparing the calculated radiative lifetimes of different structures with measured values can provide additional data for discriminating between candidate structures.

Table 1 summarizes the calculated HOMO–LUMO gaps of each cluster. Previous calculations [40] have shown that it is not possible to directly compare DFT-LDA calculated gaps of doped silicon nanoclusters with experimental gaps for two reasons:

(i) DFT calculated gaps of Si nanoclusters may underestimate the true optical gap;
(ii) gaps calculated with a single surface dopant typically overestimate the gap compared to clusters covered with multiple surface dopants.

However, the qualitative changes in the gap of nanoclusters with different surface dopant structures have been shown to be well reproduced by DFT calculations in studies of oxygen terminated Si nanoclusters [40]. In figure 4 the measured onset of absorption is approximately 2 eV. This is considerably lower than the 3.4 eV gap of our reference crystalline structure, $Si_{35}H_{36}$, and also slightly lower than the 2.2 eV gap of the hydrogen terminated amorphous structure. As we expect these DFT calculated absorption gaps to underestimate experimental values, it is unlikely that the absorption in SRN materials is occurring in the cores of either crystalline or amorphous, pure silicon clusters. However, for both the crystalline and amorphous clusters, addition of N significantly lowers the calculated gaps and the smallest gaps are found when N is added on the surface of the cluster. This suggests that absorption and emission may originate at the interface between the Si cluster and the SRN matrix rather than from the core of the nanoclusters. The HOMO and LUMO orbital densities of each cluster are shown in figure 7. In our reference crystalline and amorphous clusters, (a) and (h), both the HOMO and LUMO orbitals are delocalized throughout the core of the cluster. Upon addition of nitrogen, the HOMO orbital becomes localized around the nitrogen atom and exhibits a *p* character. Analysis of the individual HOMO and LUMO eigenvalues shows that the gap of these clusters is reduced because the nitrogen localized HOMO states are higher in energy than the HOMO of the reference hydrogen terminated clusters. Also included in table 1 are our calculated radiative lifetimes. These lifetimes, τ, are evaluated using the methodology described in [26]. In figure 7, structures (b), (d), (e) and (j) have large radiative lifetimes for their lowest transitions.

In structure (d), the HOMO–LUMO transition is forbidden by symmetry and the lowest allowed transition is the HOMO to LUMO + 1. For structures (b) and (e), the high atomic symmetry of the nitrogen groups is slightly broken by structural relaxations, such as the rotation of an N–H bond, yielding only a weak oscillator strength. For structure (j) the low oscillator strength and hence long radiative lifetime arises from the small overlap between the HOMO and LUMO, which are localized in different regions of the cluster. Structure (f) has the shortest lifetime, an order of magnitude lower than the reference $Si_{35}H_{36}$ cluster and at least one order of magnitude lower than any other structure. We note that in addition to radiative recombination of carriers, we also expect significant non-radiative carrier decay and therefore the radiative lifetime should be considered an upper bound to the measured lifetime.

Combining our first-principles calculations and experimental measurements we can constrain the range of structures responsible for luminescence in SRN. Structures (f) and (j) with nitrogen bridged between two bonded Si atoms have the lowest gaps for the crystalline and amorphous structures, respectively, and are closest to the measured gaps. If one also considers the radiative lifetime, structure (f) is the only structure exhibiting both a short radiative lifetime and the onset of absorption consistent with our experimental results.

5. Energy transfer to lead sulphide (PbS) quantum dots

Luminescence from colloidal quantum dots is very efficient and widely tuneable in wavelength. Coupling silicon-based materials with colloidal quantum dots would greatly enrich silicon's growing set of functionalities. In the following we will review our recent work [42] that has demonstrated up to 60% efficiency in non-radiative energy transfer from SRN materials to light-emitting PbS colloidal quantum dots. The result suggests a convenient integration of solution-processible active optoelectronic materials (PbS quantum dots) on the electronics platform of silicon-based technology. In particular, the large overlap of the SRN luminescence spectrum with the absorption spectrum of PbS quantum dots, as demonstrated in figure 9 below, suggests a novel opportunity for energy coupling of these two promising optoelectronic materials.

We have investigated energy transfer between SRN and PbS quantum dots by measuring photoluminescence excitation spectra (PLE) of three samples: the proximately coupled donor–acceptor sample (Sample A), the donor–spacer–acceptor sample (Sample C), and the acceptor-only reference sample (Sample B), as shown in figure 8.

In this study, the first excitonic peak of the PbS quantum dots is manifested on the absorption curve at 1300 nm (figure 9). The PbS quantum dot photoluminescence spectrum (figure 9 dash line) is Stokes-shifted to 1400 nm. These optical properties of the PbS quantum dots are given by dots with average size of 5 nm, as shown in the electron micrograph in figure 8. We produced the proximately coupled donor–acceptor sample by spin-coating five monolayers of PbS QDs (about 25 nm film thickness) on 50 nm of SRN grown on a transparent quartz substrate. The reference sample was identical except that the QDs were spin-cast onto a transparent quartz substrate. In the donor–spacer–acceptor structure, a 1 mm transparent quartz

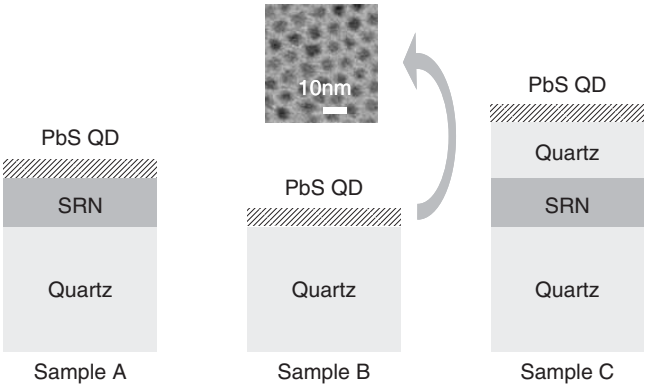

Figure 8. Structure of samples. (A) The proximately coupled donor–acceptor sample. (B) The acceptor-only reference sample. (C) The donor–spacer–acceptor sample. The inset shows a TEM image of the PbS QDs. Average diameter is about 5 nm.

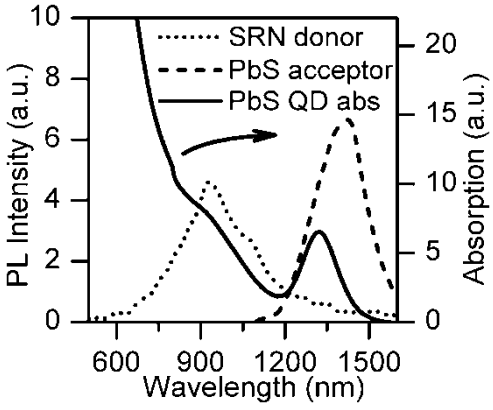

Figure 9. Absorption spectrum of PbS QD (solid line). Room-temperature photoluminescence spectrum of 50 nm thick SRN (dot line) on a quartz substrate and that of PbS QD on a quartz substrate (dash line).

spacer was introduced between the PbS QD acceptor layer and the 50 nm SRN donor layer to prevent short-range dipole coupling while still allowing radiative coupling.

In the PLE experiment (figure 10) the excitation wavelength was varied between 390 and 560 nm while the detection wavelength was fixed at the PbS QD emission peak. Photoluminescence excitation spectra of the samples along with the SRN absorption spectrum are shown in figure 10. For excitation wavelengths longer than 500 nm where the SRN absorption is negligible, the PLE spectra overlap for all samples. This is the regime of direct PbS QD excitation alone, producing conventional photoluminescence. For excitation at wavelengths shorter than 500 nm, the photoluminescence of the proximately coupled donor–acceptor sample rises significantly, while the reference sample and the donor–spacer–acceptor sample overlap one another and do not rise. It is concluded that the factor-of-two luminescence enhancement of PbS QDs coupled

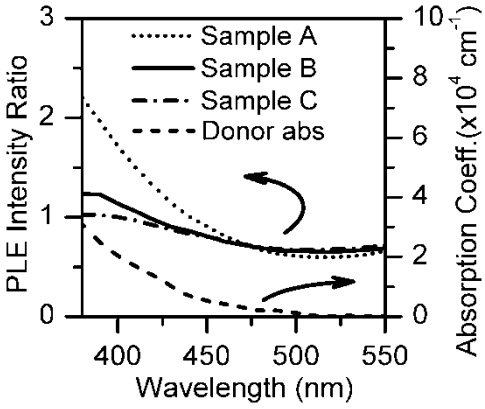

Figure 10. PLE trace of the acceptor-only reference sample (Sample B, solid line), the donor–spacer–acceptor sample (Sample C, dash-dot line), and the proximately coupled donor–acceptor sample (Sample A, dot line). Absorption spectrum of 50 nm thick SRN (donor) on a quartz substrate is also shown (dash line).

to the SRN thin film donor is dominated by a short-distance, non-radiative energy transfer process.

This finding points to the possibility of a convenient coupling and thus monolithic integration of solution-processible near-infrared-active optoelectronic materials on the electronics platform of CMOS silicon.

6. Energy transfer to erbium ions

The recent discovery of efficient energy transfer between silicon nanocrystals (Si-nc's) and Er ions has initiated an entirely new approach that profits from both the advantages of quantum size effects in Si and rare earth doping, promising a route towards the integration of CMOS technology with 1.54 m light sources [43–48].

In particular, Er-doped SRO systems (Er : SRO) have been extensively investigated and we recently demonstrated very efficient energy sensitization also for low-temperature annealed (600–800°C) Er : SRO samples produced by magnetron co-sputtering [46]. The typical mechanism used to explain energy transfer between Si-nc's and Er ions is Förster–Dexter non-radiative energy coupling with a transfer rate that is directly proportional to the donor (SRO) emission rate [47]. However, we have recently questioned the validity of this simple picture since only inefficient light emission (no appreciable SRO emission rate) can be obtained in the case of low-temperature annealed samples (donors) without the presence of Er atoms (acceptor) [46, 48]. We have recently suggested that the efficient energy transfer observed for low-temperature annealed Er : SRO materials can be assisted by non-radiative defect states within the SRO matrix bandgap [48].

We have discovered that a very similar picture also applies for the case of Er : SRN systems, opening the possibility to extend the emission wavelength range of SRN optical devices to the strategically relevant 1.54 m region due to efficient energy transfer

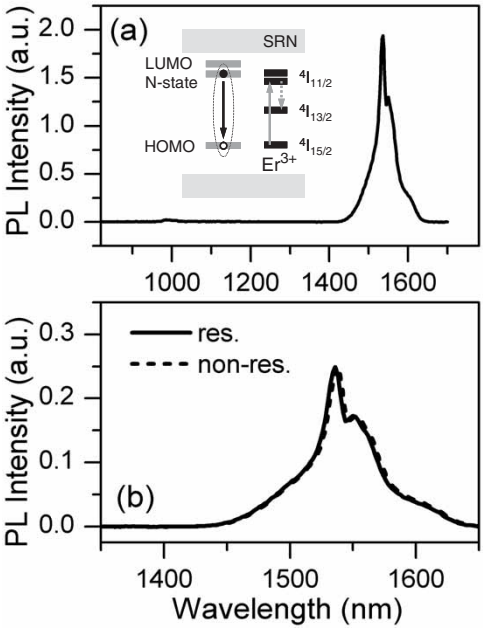

Figure 11. (a) Room-temperature photoluminescence of sputtered Er : SRN sample. The refractive index of the Er : SRN sample is 2.25 and the emission is excited at 488 nm with 10 mW. (Inset) Schematic diagram illustrating the erbium and nitrogen passivated Si-clusters energy levels. (b) Room-temperature photoluminescence of Er : SRN system with resonant (488 nm, solid line) and non-resonant (457 nm, dash line) excitation.

to erbium ions. In figure 11 we clearly show that 1.54 m Er-related emission can be efficiently excited also by pumping out of the Er transitions resonance, using a pumping wavelength (457 nm) where Er ions are non-absorbing (figure 11b). The almost totally overlapping Er emission spectra obtained under resonant (488 nm) and non-resonant (457 nm) pumping conditions directly show that Er excitation in Er : SRN is completely mediated by the SRN dielectric matrix that efficiently transfers the excitation energy to the Er ions, as schematically shown in the inset of figure 11(a). Further investigations are in progress to clarify the nature of this novel energy transfer phenomena.

7. Complex photonic structures and aperiodic waveguides

The high refractive index ($n = 2.23$) of PE-CVD deposited Si-rich silicon nitride (SRN) and its ability to efficiently emit, when thermally annealed, intense near-infrared light with little reabsorption losses (due to strong absorption/emission Stokes shift) represent very attractive features that make the SRN material suitable for the fabrication of high-quality active (light-emitting) photonic structures. In particular, CMOS-compatible active waveguides and complex photonic crystal structures can be easily fabricated and are appealing for a variety of different applications ranging from

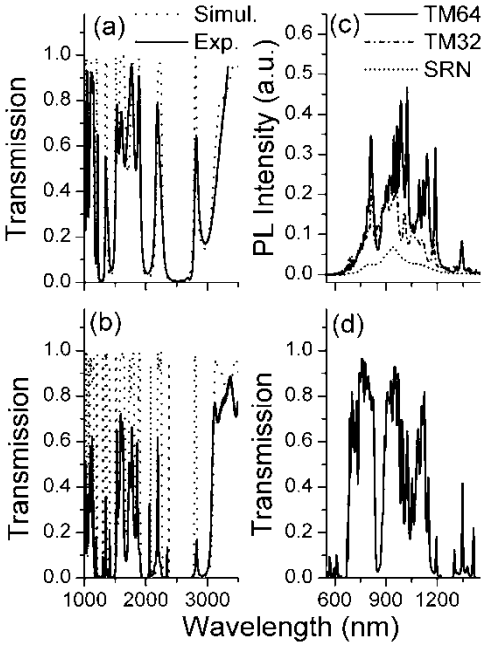

Figure 12. (a) Experimental (solid line) and calculated (dot line) transmission for the 32 layer T–M structure (TM32). (b) Experimental (solid line) and calculated (dot line) transmission for the 64 layer T–M structure (TM64). For all the simulations we have considered $n_A = 2.23$ (SRN), $n_B = 1.45$ (SiO_2). The thickness simulation parameters that yield the best fit with the experimental transmission data are $d_A = 198.9$ nm and $d_B = 273$ nm, which are approximately 6% thicker and 4% thinner than the targeted values defined by the Bragg condition at $_0 = 1.65$ m. (c) Room-temperature photoluminescence (PL) intensity of a TM64 sample (solid line), a TM32 sample (dash-dot line), and a homogeneous SRN reference sample (dot line). The excitation wavelength was 488 nm and the pump power was 10 mW. (d) Experimental transmission spectrum for the 64 layer T–M structure overlapping the light-emission range of the SRN material.

innovative resonant structures for on-chip light amplification and lasing, to optical biosensing and dense optical wavelength division multiplexing (WDM).

We have recently fabricated the first light-emitting Thue–Morse (T–M) photonic multilayers structure by aperiodically arranging SRN and SiO_2 layers grown by PE-CVD [25]. The complex photonic crystal structure is fabricated by stacking SRN layers (A layers) and SiO_2 layers (B layers) according to the Thue–Morse aperiodic sequence generated by the simple inflation rule: σ_{T-M}: AAB, BBA [49]. The complexity of the T–M sequence, reflected by its singular continuous Fourier transform, induces an 'almost random' dielectric environment where the diffusion of light waves can undergo a power-law (weak) localization and large field enhancement at specific frequencies corresponding to perfect transmission states (resonant transmission) can occur [50, 51]. The optical transmission spectra of thermally annealed photonic T–M structures with up to 64 layers (TM64) are shown in figure 12. In figure 12(c) we show the photoluminescence spectra of the light-emitting T–M structures. Very sharp emission peaks induced by the aperiodic light scattering in the T–M environment are clearly distinguishable for the TM64 structure (solid line). More interestingly, we have recently shown [25] that light emission can be resonantly enhanced (with respect to a reference

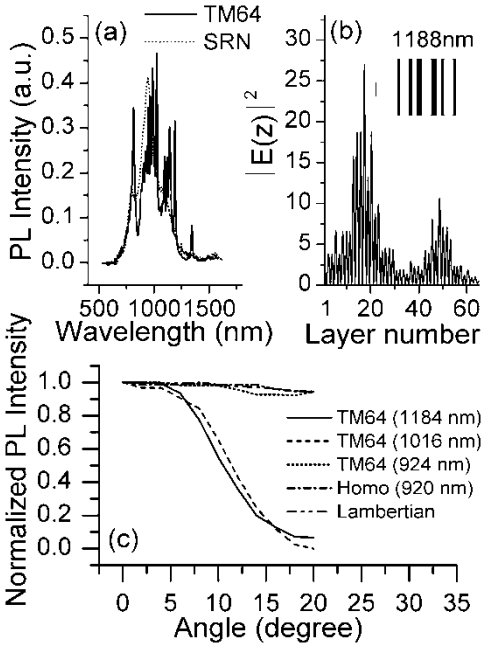

Figure 13. (a) Comparison of the TM64 emission spectrum (solid line) and the homogeneous reference sample emission spectrum (dot line) rescaled according to the SRN thickness ratio. (b) One-dimensional (1D) transfer matrix calculation of the T–M state field intensity distribution at 1188 nm. The inset shows a sketch of the multilayer T–M structure with normalized plane waves entering from the left. (c) Angular profile of the normalized emitted intensity of T–M (64 layers) at different wavelengths indicated in the figure and for the reference homogeneous SRN sample.

SRN homogeneous sample) at multiple wavelengths for a light-emitting T–M structure [25]. In figure 13(a) we compare the emission spectra of a TM64 structure and a homogeneous SRN reference sample with the same optical thickness. We notice that the presence of an aperiodic dielectric environment dramatically modifies the broad and featureless emission band characteristic of the SRN reference sample. In particular, several narrow frequency states (emission spikes) are induced by the T–M structure and the associated emission intensity is locally enhanced with respect to the reference homogeneous SRN sample. A one-dimensional transfer matrix simulation of a T–M localized field state is shown in figure 13(b). Field enhancement effects up to approximately 30 times the incident field amplitude are predicted for the TM64 structure. Moreover, the localized character of these states is also reflected in the dramatic change of the angular emission profile of the T–M structure. Figure 13(c) shows the strongly directional light emission observed for the T–M structures at different wavelengths corresponding to localized states with field enhancement. For the SRN homogeneous sample, an approximately Lambertian wide-angle emission profile was observed since all the states are delocalized with negligible field enhancement.

The demonstration of broad-band light-emitting T–M structures with highly directional and multiple-wavelength emission enhancement effects can provide an

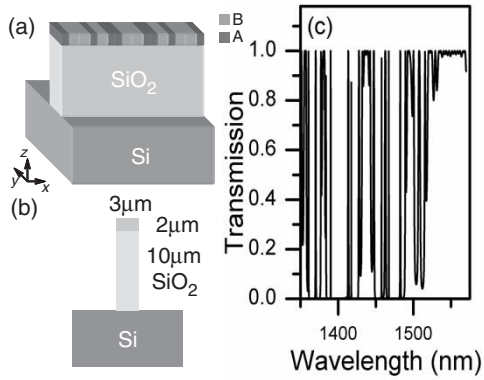

Figure 14. (a) Schematics of a planar Thue–Morse aperiodic waveguide device. A and B represents different dielectric materials. For our simulations we have chosen A = SRN with $n_A = 2.2$ and B = SON with $n_B = 1.7$. (b) Cross-section of the device, and (c) calculated transmission spectrum for the light that propagates through the aperiodic waveguide.

attractive route towards the fabrication of optically active CMOS devices for multiwavelength operation.

In the following we will introduce the novel concept and design of a CMOS-compatible, SRN-based waveguide structure that guides light due to the excitation of multiple resonant transmission states induced by the aperiodic dielectric environment. In figure 14(a,b) we show the schematics of the aperiodic waveguide structure module that we have considered. Within this flexible module, we can easily change the aperiodic character of the guiding subunits by simply considering different generation sequences. In the following, we studied the light propagation in the two chiefly aperiodic environments: the Thue–Morse and the Rudin–Shapiro sequences [52]. The binary sequence of Rudin–Shapiro (R–S) shows fascinating new physical properties [53, 54] and can be generated by a substitution rule acting on a four-letter alphabet $\{a, b, c, d\}$, which is then reduced to a sequence of two letters. A binary substitution relation is defined by the form $a \rightarrow ab$, $b \rightarrow ac$, $c \rightarrow db$, $d \rightarrow dc$ [51]. If A is used as a seed and applied to the substitution once, the first generation of the sequence will be obtained. The first few generations are: $s_0 = \{a\}$, $s_1 = \{ab\}$, $s_2 = \{abac\}$, $s_3 = \{abacabdb\}$. The R–S sequence is obtained after identifying each a and b with A and each c and d with B. The third generation will then be $S_3 = \{AAABAABA\}$, and so on. The photonic structures that we have studied are as follows: on top of an SiO_2 undercladding (10 m thick) we have designed a Thue–Morse or R–S aperiodic sequence of SRN ($n = 2.2$) and silicon oxynitride (SON) layers ($n = 1.7$) with $3\lambda_0/4$ optical length and $\lambda_0 = 1.55$ nm. This corresponds to a physical subunit length of d_{SRN}539 nm and d_{SON}704 nm, respectively, when the effective refractive indices are considered. The device cross-section is shown in figure 14(b). For these optimized design choices, the optical modes are perfectly matched for the different subunits and the waveguide device can be easily fabricated using standard photolithography and etching steps. We have calculated the transmission spectrum of the aperiodic waveguide by using a commercially available three-dimensional mode solver package based on mode matching techniques. The Photon Design *FimmWave* software was used for optimization of the modal overlap

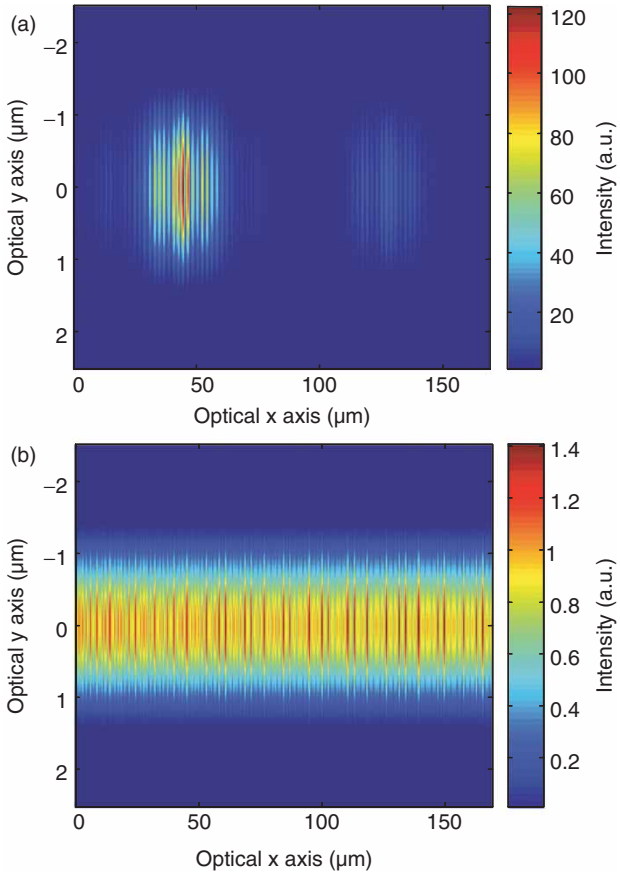

Figure 15. (a) Calculated electric field profile in the waveguide showing a localized T–M state at 1390 nm. (b) Calculated electric field profile in the horizontal plane of the waveguide showing an extended T–M state at 1550 nm. This figure is available in colour online.

in the waveguide subunits and the *FimmProp* framework code was used to simulate the mode propagation. The optical transmission of the Thue–Morse waveguide with up to 256 SRN/SON subunits is shown in figure 14(c). The waveguide transmission spectrum is very similar to the spectra of the strictly one-dimensional system that we considered in figure 12. However, for the waveguide structure, a bigger field enhancement effect can be achieved due to a much longer scattering length along the propagation axis. The calculated electric field distribution in the waveguide structure is shown in figure 15 for two different T–M modes. In this specific example, a strongly localized mode (figure 15a) yields a resonant transmission state at the wavelength (1390 nm) corresponding to a largely enhanced electric field (up to 80 times the incident field) in the structure. On the other hand, extended Thue–Morse states (with no field enhancement, 1550 nm) coexist in the structure (figure 15b) and propagate through the waveguide without experiencing field enhancement effects. We emphasize that the aperiodic waveguide module introduced in figure 14 can easily be generalized to study light propagation in different aperiodic environments. For example, in figure 16 we

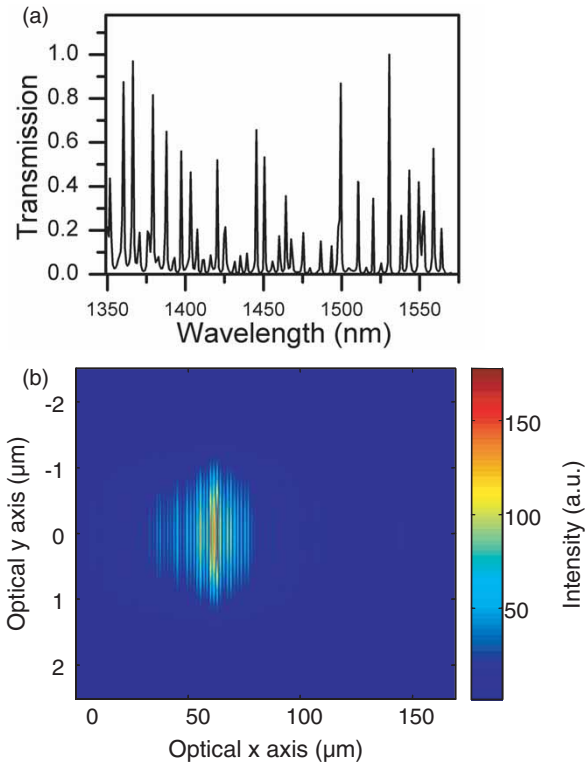

Figure 16. (a) Calculated optical transmission of the Rudin–Shapiro aperiodic waveguide. (b) Simulation of the electric field profile in the horizontal plane of the waveguide showing a localized R–S state at 1487 nm. This figure is available in colour online.

have calculated the transmission (a) and the electric field distribution (b) of the more general R–S structure, that has the remarkable property of an absolutely continuous Fourier spectrum (more disorder) that creates strongly localized and enhanced optical fields (figure 16b). This study demonstrates that resonant effects associated with field enhancement in localized light modes can provide an alternative mechanism to transport light waves over large distances and with strong light–matter coupling (field enhancement). The fabrication of proof-of-concept resonant aperiodic waveguide structures is currently in progress.

8. Conclusions

In this paper we have shown our main results on the optical emission characteristics of SRN nanostructures for microphotonic applications. In particular, we have demonstrated the presence of small (1–2 nm) Si clusters embedded in the amorphous nitride matrix, yielding 7% efficient and largely Stokes-shifted near-infrared emission with nanosecond recombination dynamics and negligible thermal quenching. We have performed first-principles calculations on 1 nm Si dots suggesting that light emission

originates from nitrogen-related, strongly localized exciton transitions at the surface of small amorphous Si clusters. In addition, we have demonstrated energy sensitization from SRN to erbium ions and to colloidal PbS quantum dots, opening a convenient strategy for the monolithic integration of solution-processible active optoelectronic materials on the electronics platform of CMOS silicon. Finally, we have shown that light-emitting SRN is a suitable material for the fabrication of optically active complex photonic crystals structures and novel waveguide structures based on the excitation of field-enhanced resonant transmission states in aperiodic dielectrics. The versatility of light-emitting SRN systems can provide alternative routes towards the fabrication of optically active CMOS devices.

Acknowledgements

We thank Dr. X. Duan for TEM sample preparation and imaging. This work has been supported by the MRSEC Program of the National Science Foundation under Contract No. DMR 02-13282. The work made use of MRSEC Shared Facilities supported by the SNF under Award Number DMR-0213282 and NSF Laser Facility Grant CHE-0111370. The LLNL work was performed under the auspices of the US Department of Energy by the University of California, Lawrence Livermore National Laboratory under contract No. W-7405-Eng-48.

References

[1] J. S. Foresi, P. R. Villeneuve, J. Ferrera, E. R. Thoen, G. Steinmeyer, S. Fan, J. D. Joannopoulos, L. C. Kimerling, H. I. Smith, and E. P. Ippen. Photonic-bandgap microcavities in optical waveguides. Nature **390,** 143 (1997).
[2] D. K. Armani, T. J. Kippenberg, S. M. Spillane, and K. J. Vahala. Ultra-high-*Q* toroid microcavity on a chip. Nature **421,** 925 (2003).
[3] A. Polman, B. Min, J. Kalkman, T. J. Kippenberg, and K. J. Vahala. Ultralow-threshold erbium-implanted toroidal microlaser on silicon. Appl. Phys. Lett. **84,** 1037 (2004).
[4] A. Liu, R. Jones, L. Liao, D. Samara-Rubio, D. Rubin, O. Cohen, R. Nicolaescu, and M. Paniccia. A high-speed silicon optical modulator based on a metal–oxide–semiconductor capacitor. Nature **427,** 615 (2004).
[5] V. R. Almeida, C. A. Barrios, R. R. Panepucci, and M. Lipson. All-optical control of light on a silicon chip. Nature **431,** 1081 (2004).
[6] O. Boyraz and B. Jalali. Demonstration of a silicon Raman laser. Opt. Express **12,** 5269 (2004).
[7] H. Rong, A. Liu, R. Jones, O. Cohen, D. Hak, R. Nicolaescu, A. Fang, and M. Paniccia. An all-silicon Raman laser. Nature **433,** 292 (2005).
[8] L. T. Canham. Silicon quantum wire array fabrication by electrochemical and chemical dissolution of wafers. Appl. Phys. Lett. **57,** 1046 (1990).
[9] Z. H. Lu, D. J. Lockwood, and J. M. Baribeau. Quantum confinement and light emission in SiO_2/Si superlattices. Nature **378,** 258 (1995).
[10] K. D. Hirschman, L. Tsybeskov, S. P. Duttagupta, and P. M. Fauchet. Silicon-based visible light-emitting devices integrated into microelectronic circuits. Nature **384,** 338 (1996).
[11] *Towards the First Silicon Laser,* NATO Advanced Studies Institute, Series 11, edited by L. Pavesi, S. Gaponenko, and L. Dal Negro (Kluwer Academic, Dordrecht, 2003) Vol 93.
[12] *Silicon Photonics,* edited by L. Pavesi and D. J. Lockwood (Springer-Verlag, Berlin, 2004).
[13] B. Gelloz, A. Kojima, and N. Koshida. Highly efficient and stable luminescence of nanocrystalline porous silicon treated by high-pressure water vapor annealing. Appl. Phys. Lett. **87,** 031107 (2005).
[14] L. Pavesi, L. Dal Negro, C. Mazzoleni, G. Franzò, and F. Priolo. Optical gain in silicon nanocrystals. Nature **408,** 440 (2000).

[15] L. Khriachtchev, M. Rasanen, S. Novikov, and J. Sinkkonen. Optical gain in Si/SiO_2 lattice: experimental evidence with nanosecond pulses. Appl. Phys. Lett. **79,** 1249 (2001).
[16] L. Dal Negro, M. Cazzanelli, L. Pavesi, S. Ossicini, D. Pacifici, G. Franzò, F. Priolo, and F. Iacona. Dynamics of stimulated emission in silicon nanocrystals. Appl. Phys. Lett. **82,** 4636 (2003).
[17] J. Ruan, P. M. Fauchet, L. Dal Negro, M. Cazzanelli, and L. Pavesi. Stimulated emission in nanocrystalline silicon superlattices. Appl. Phys. Lett. **83,** 5479 (2003).
[18] L. Dal Negro, M. Cazzanelli, B. Danese, L. Pavesi, F. Iacona, G. Franzò, and F. Priolo. Light amplification in silicon nanocrystals by pump and probe transmission measurements. J. Appl. Phys. **96,** 5747 (2004).
[19] M. Cazzanelli, D. Kovalev, L. Dal Negro, Z. Gaurro, and L. Pavesi. Polarized optical gain and polarization-narrowing of heavily oxidized porous silicon. Phys. Rev. Lett. **93,** 207402 (2004).
[20] M. Fujii, M. Yoshida, Y. Kanzawa, S. Hayashi, and K. Yamamoto. 1.54 μm photoluminescence of Er^{3+} doped into SiO_2 films containing Si nanocrystals: evidence for energy transfer from Si nanocrystals to Er^{3+}. Appl. Phys. Lett. **71,** 1198 (1997).
[21] G. Franzò, F. Icona, V. Vinciguerra, and F. Priolo. Enhanced rare earth luminescence in silicon nanocrystals. Mater. Sci. Eng. B **69/70,** 335 (2000).
[22] F. Priolo, G. Franzò, F. Iacona, D. Pacifici, and V. Vinciguerra. Excitation and non-radiative de-excitation processes in Er-doped Si nanocrystals. Mater. Sci. Eng. B **81,** 9 (2001).
[23] N. M. Park, C. J. Choi, T. Y. Seong, and S. J. Park. Quantum confinement in amorphous silicon quantum dots embedded in silicon nitride. Phys. Rev. Lett. **86,** 1355 (2001).
[24] K. S. Cho, N. M. Park, T. Y. Kim, K. H. Kim, G. Y. Sung, and J. H. Shin. High efficiency visible electroluminescence from silicon nanocrystals embedded in silicon nitride using a transparent doping layer. Appl. Phys. Lett. **86,** 071909 (2005).
[25] L. Dal Negro, J. H. Yi, V. Nguyen, Y. Yi, J. Michel, and L. C. Kimerling. Spectrally enhanced light emission from aperiodic photonic structures. Appl. Phys. Lett. **86,** 261905 (2005).
[26] L. Dal Negro, J. H. Yi, L. C. Kimerling, S. Hamel, A. Williamson, and G. Galli. Light emission from silicon-rich nitride nanostructures. Appl. Phys. Lett. (submitted).
[27] M. A. Hines and G. D. Scholes. Colloidal PbS nanocrystals with size-tunable near-infrared emission: observation of post-synthesis self-narrowing of the particle size distribution. Adv. Mater. **15,** 1844 (2003).
[28] I. H. Campbell and P. M. Fauchet. The effects of microcrystal size and shape on the one phonon Raman spectra of crystalline semiconductors. Solid State Comm. **58,** 739 (1986).
[29] Y. Kanemitsu, H. Uto, Y. Masumoto, T. Matsumoto, T. Futagi, and H. Mimura. Microstructure and optical properties of free-standing porous silicon films: Size dependence of absorption spectra in Si nanometer-sized crystallites. Phys. Rev. B **48,** 2827 (1993).
[30] P. Mishra and K. P. Jain. First- and second-order Raman scattering in nanocrystalline silicon. Phys. Rev. B **64,** 073304 (2001).
[31] T.-W. F. Chang, A. Maria, P. W. Cyr, V. Sukhovatkin, L. Levina, and E. H. Sargent. High near-infrared photoluminescence quantum efficiency from PbS nanocrystals in polymer films. Synthetic Metals **148,** 257 (2005).
[32] J. C. de Mello, H. F. Wittmann, and R. H. Friend. An improved experimental determination of external photoluminescence quantum efficiency. Adv. Mater. **9,** 230 (1997).
[33] L. Dal Negro, J. H. Yi, L. C. Kimerling, T.-W. F. Chang, V. Sukhovatkin, and E. H. Sargent. Light emission efficiency and dynamics in silicon-rich silicon nitride films. Appl. Phys. Lett. (submitted).
[34] S. V. Deshpande, E. Gulari, S. W. Brown, and S. C. Rand. Optical properties of silicon nitride films deposited by hot filament chemical vapor deposition. J. Appl. Phys. **77,** 6534 (1995).
[35] The Qbox [36] code was used for the structural relaxation and the ABINIT[37] code was used to evaluate gaps and oscillator strength. All calculations use norm conserving, Troullier-Martins pseudopotentials for the core electrons and a plane-wave basis with a 70 Ry cutoff.
[36] F. Gygi. Lawrence Livermore National Laboratory. internal communication.
[37] The ABINIT code is a common project of the Université Catholique de Louvain, Corning Incorporated, and other contributors (URL http://www.abinit.org).
[38] D. M. Ceperley and B. J. Alder. Ground state of the electron gas by a stochastic method. Phys. Rev. Lett. **45,** 566 (1980).
[39] E. W. Draeger, J. C. Grossman, A. J. Williamson, and G. Galli. Influence of synthesis conditions on the structural and optical properties of passivated silicon nanoclusters. Phys. Rev. Lett. **90,** 167402 (2003).
[40] S.-H. Lee and M.-H. Kang. First-principles study of the dissociative adsorption of NH_3 on the Si(100) surface. Phys. Rev. B **58,** 4903 (1998).
[41] S. Bengio, H. Ascolani, N. Franco, J. Avila, M. C. Asensio, A. M. Bradshaw, and D. P. Woodruff. Local structure determination of NH_2 on Si(111)-(7×7). Phys. Rev. B **69,** 125340 (2004).
[42] A. Puzder, A. J. Williamson, J. C. Grossman, and G. Galli. Surface control of optical properties in silicon nanoclusters. J. Chem. Phys. **117,** 6721 (2002).

[43] Landolt-Börnstein. Numerical data and functional relationships in science and technology. In *Structure Data of Free Polyatomic Molecules*, edited by K.-H. Hellwege and A. M. Hellwege (Springer-Verlag, New York, 1976) Vol. 7.
[44] T.-W.F. Chang, L. Dal Negro, V. Sukhovatkin, J. H. Yi, L. C. Kimerling, and E. H. Sargent. Efficient energy transfer from silicon-based thin films to colloidal PbS quantum dots. Appl. Phys. Lett. (submitted).
[45] A. J. Kenyon, P. F. Trwoga, M. Federighi, and C. W. Pitt. Optical properties of PECVD erbium-doped silicon-rich silica: evidence for energy transfer between silicon microclusters and erbium ions. J. Phys. Condens. Matter **6,** L319 (1994).
[46] M. Fujii, M. Yoshida, Y. Kanzawa, S. Hayashi, and K. Yamamoto. 1.54 μm photoluminescence of Er^{3+} doped into SiO_2 films containing Si nanocrystals: evidence for energy transfer from Si nanocrystals to Er^{3+}. Appl. Phys. Lett. **71,** 1198 (1997).
[47] G. Franzò, V. Vinciguerra, and F. Priolo. The excitation mechanism of rare-earth ions in silicon nanocrystals. Appl. Phys. A **69,** 3 (1999).
[48] M. Stolfi, L. Dal Negro, J. Michel, X. Duan, J. LeBlanc, J. Haavisto, and L. C. Kimerling. CMOS compatible erbium coupled silicon nanocrystals thin films for microphotonics. Mater. Res. Soc. Symp. Proc. **832** (2005).
[49] T. Miyakawa and D. L. Dexter. Phonon Sidebands, Multiphonon relaxation of excited states, and phonon-assisted energy transfer between ions in solids. Phys. Rev. B **1,** 2961 (1970).
[50] L. Dal Negro, M. Stolfi, J. Michel, J. LeBlanc, J. Haavisto, and L. C. Kimerling. A comparative study of energy transfer from substoichiometric oxides to Erbium ions. Appl. Phys. Lett. (in preparation).
[51] Niam-hua Liu. Propagation of light waves in Thue-Morse dielectric multilayers. Phys. Rev. B **55,** 3543 (1997).
[52] P. E. de Brito, C. A. A. Da Silva, and N. H. Nazareno. Field-induced localization in Fibonacci and Thue-Morse lattices. Phys. Rev. B **51,** 6096 (1995).
[53] M. Dulea, M. Johansson, and R. Riklund. Localization of electrons and electromagnetic waves in a deterministic aperiodic system. Phys. Rev. B **45,** 105 (1992).
[54] L. Kroon, E. Lennholm, and R. Riklund. Localization-delocalization in aperiodic systems. Phys. Rev. B **66,** 094204 (2002).
[55] F. Igloi, L. Turban, and H. Rieger. Anomalous diffusion in aperiodic environments. Phys. Rev. E **59,** 1465 (1999).
[56] L. Kroon and R. Riklund. Absence of localization in a model with correlation measure as a random lattice. Phys. Rev. B **69,** 094204 (2004).
[57] The Photon Design *FimmWave* software was used for optimization of the modal overlap in the waveguide sub-units and the *FimmProp* framework code was used to simulate the mode propagation.